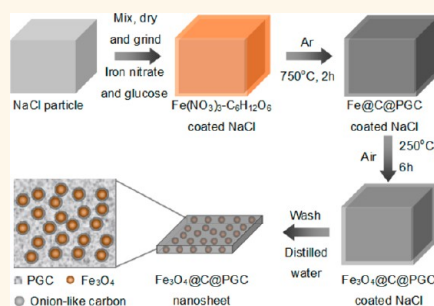# Carbon-Encapsulated Fe_3O_4 Nanoparticles as a High-Rate Lithium Ion Battery Anode Material

Chunnian He, Shan Wu, Naiqin Zhao,* Chunsheng Shi, Enzuo Liu, and Jiajun Li

School of Materials Science and Engineering and Tianjin Key Laboratory of Composites and Functional Materials, Tianjin University, Tianjin 300072, People's Republic of China

ABSTRACT A facile and scalable *in situ* synthesis strategy is developed to fabricate carbon-encapsulated Fe_3O_4 nanoparticles homogeneously embedded in two-dimensional (2D) porous graphitic carbon nanosheets (Fe_3O_4@C@PGC nanosheets) as a durable high-rate lithium ion battery anode material. With assistance of the surface of NaCl particles, 2D Fe@C@PGC nanosheets can be *in situ* synthesized by using the $Fe(NO_3)_3 \cdot 9H_2O$ and $C_6H_{12}O_6$ as the metal and carbon precursor, respectively. After annealing under air, the Fe@C@PGC nanosheets can be converted to Fe_3O_4@C@PGC nanosheets, in which Fe_3O_4 nanoparticles (~18.2 nm) coated with conformal and thin onion-like carbon shells are homogeneously embedded in 2D high-conducting carbon nanosheets with a thickness of less than 30 nm. In the constructed architecture, the thin carbon shells can avoid the direct exposure of encapsulated Fe_3O_4 to the electrolyte and preserve the structural and interfacial stabilization of Fe_3O_4 nanoparticles. Meanwhile, the flexible and conductive PGC nanosheets can accommodate the mechanical stress induced by the volume change of embedded Fe_3O_4@C nanoparticles as well as inhibit the aggregation of Fe_3O_4 nanoparticles and thus maintain the structural and electrical integrity of the Fe_3O_4@C@PGC electrode during the lithiation/delithiation processes. As a result, this Fe_3O_4@C@PGC electrode exhibits superhigh rate capability (858, 587, and 311 mAh/g at 5, 10, and 20 C, respectively, 1 C = 1 A/g) and extremely excellent cycling performance at high rates (only 3.47% capacity loss after 350 cycles at a high rate of 10 C), which is the best one ever reported for an Fe_3O_4-based electrode including various nanostructured Fe_3O_4 anode materials, composite electrodes, *etc.*

There is an urgent requirement to develop rechargeable lithium ion batteries (LIBs) with high energy density and power density for application in hybrid electric vehicles (HEVs) and electric vehicles (EVs).[1,2] However, commercial graphite anode used currently has already reached its theoretical limit (372 mAh/g), and exploring alternative anode materials with higher charge/discharge rate and reversible capacity as well as long cycle life, low cost, and the ability to be produced at large scale has become an urgent task nowadays. In this context, transition metal oxides (MO_x, M: Fe, Co, Ni, *etc.*), which possess remarkably higher capacities (>600 mAh/g) than that of the current commercial anode material (graphite), have been extensively exploited as anode materials for high-performance LIBs.[3,4] The capacity of lithium storage is mainly achieved through the reversible conversion reaction between lithium ion and MO_x, forming metal nanocrystals dispersed in Li_2O matrix.[3,4] Despite those intriguing features, the main obstacle in developing MO_x-based anodes lies in the severe volume change of MO_x particles during lithium ion insertion/extraction, which can result in pulverization of the initial particle morphology and cause the breakdown of electrical connection of such anode materials from current collectors, thereby leading to poor cycling performance. In addition, the low electrical conductivity of pristine MO_x challenges the achievement of high capacity at high charge/discharge rates.[3,4]

In order to circumvent the above intractable problems, two typical approaches have been developed. One way is to synthesize nanostructured MO_x materials with various morphologies, including nanoparticles, nanosheets, nanowires, nanorods, nanotubes, and hollow nanostructures.[5−11] It is, in fact, expected that the passage from bulk to

©2013 American Chemical Society

nanostructures results in shorter path lengths for the transport of electrons and lithium ions, which lead to good conductivity and fast charge/discharge rates. Furthermore, these nanomaterials can accommodate the mechanical strain of lithium ion insertion/extraction much better than that of bulk materials. Nevertheless, owing to the high surface-to-volume ratio and large surface free energy of the nanostructures, the undesirable side reactions and the formation of thick solid electrolyte interphase (SEI) films can occur easily on their surfaces, which consume much of the lithium supplied by the cathodes and thus cause a large irreversible capacity (*i.e.*, low columbic efficiency) and poor cycle life. Moreover, several works have shown in many nanostructured MO_x materials that the thick SEI films formed during lithium insertion may decompose completely, catalyzed by transition metal generated during the lithium extraction processes, leading the surface of active materials to be cyclically exposed to the electrolyte.[5,6,10,11] This results in repeated formation/decomposition of very thick SEI films, leading to capacity fading and safety problems. Meanwhile, the damage of surface SEI also originates from the expansion and shrinkage of MO_x nanomaterials during cycles. As a result, there has been very limited success in producing MO_x nanostructured electrodes with satisfactory high specific capacity and high rate performance.[5-11] The other promising strategy is to construct hybrid electrodes composed of MO_x and carbon on the nanoscale.[12-42] A series of MO_x/carbon hybrids such as MO_x nanoparticles embedded in a porous carbon matrix or a mesoporous carbon foam,[17-21] MO_x nanospheres with carbon matrix support,[22] carbon-coated MO_x nanostructures,[11,23-28] two-dimensional (2D) graphene/MO_x,[12-16,29-40] or carbon nanosheets/MO_x hybrids[41,42] have been extensively reported. These MO_x/carbon hybrid electrodes can provide enough spaces to accommodate the serious volume change during the lithiation/delithiation processes and maintain the mechanical integrity of the composite electrode. The cycling performance of the MO_x-based anodes has been remarkably improved by using these MO_x/carbon hybrids. However, the high rate performance of these materials highly needed for HEVs and EVs is still not satisfying.[5-42] This may be attributed to the lack of favorable electronic and ion conductivity and the continuous growth of the unstable SEI films at the MO_x/electrolyte interface during cycling. Therefore, a novel design for the structure of the MO_x-based anode is highly needed to achieve both longer cycling life and higher rate performance.

Herein, we develop a facile and scalable *in situ* synthesis strategy to fabricate carbon-encapsulated Fe_3O_4 nanoparticles homogeneously embedded in 2D porous graphitic carbon nanosheets (designated as Fe_3O_4@C@PGC nanosheets) with superhigh rate performance and extremely excellent cycling stability at high rates. Fe_3O_4 was used as the model system due to its high theoretical capacity (924 mAh/g), nontoxicity, high corrosion resistance, low cost, natural abundance, and environmental friendliness.[3,4] The novel process for fabricating Fe_3O_4@C@PGC nanosheets involves *in situ* preparation of carbon-encapsulated Fe nanoparticles embedded in a 2D porous graphitic carbon nanosheet (designated as Fe@C@PGC nanosheet) precursor by using the surface of water-soluble NaCl particles as the template and calcination of the Fe@C@PGC nanosheet precursor under air. This process produces Fe_3O_4@C@PGC nanosheets in which the *in situ* synthesized Fe_3O_4 nanoparticles (~18.2 nm) coated with conformal and thin onion-like carbon shells are very homogeneously embedded in 2D high-conducting carbon nanosheets with a thickness of less than 30 nm. In this constructed unique 2D encapsulation architecture, the thin onion-like carbon shells can effectively avoid the direct exposure of encapsulated Fe_3O_4 to the electrolyte and preserve the structural and interfacial stabilization of Fe_3O_4 nanoparticles. Meanwhile, the flexible and conductive 2D PGC nanosheets can accommodate the mechanical stress induced by the volume change of embedded Fe_3O_4@C nanoparticles as well as inhibit the aggregation of Fe_3O_4 nanoparticles and thus maintain the structural and electrical integrity of the Fe_3O_4@C@PGC electrode during the charge and discharge processes. As a result, this novel 2D Fe_3O_4@C@PGC composite electrode exhibits tremendously improved rate performance compared with previous Fe_3O_4 nanostructures and Fe_3O_4/carbon hybrids and shows superhigh rate capability (858 mAh/g at 5 °C, 587 mAh/g at 10 C, and 311 mAh/g at 20 C, 1 C = 1 A/g) and extremely excellent cycling performance at high rates (only 3.47% capacity loss after 350 cycles at a high rate of 10 C), exhibiting very great potential as an extremely durable high-rate anode material for LIBs.

RESULTS AND DISCUSSION

Our approach to a novel fabrication process for 2D Fe_3O_4@C@PGC nanosheets principally consists of *in situ* synthesis and oxidation of 2D Fe@C@PGC nanosheets. As illustrated in Figure 1, this novel process is mainly composed of two steps. The first step involves producing Fe@C@PGC nanosheets by using the surface of thermally stable NaCl particles as the template and using the $Fe(NO_3)_3 \cdot 9H_2O$ and $C_6H_{12}O_6$ as the metal precursor and carbon precursor, respectively. In the synthesis, an aqueous solution of $Fe(NO_3)_3 \cdot 9H_2O$, $C_6H_{12}O_6$, and NaCl was mixed together, and the resulting mixed solution was dried and then ground to obtain very fine composite powders. During this process, *in situ* formed $Fe(NO_3)_3 - C_6H_{12}O_6$ complex was evenly coated on the surface of NaCl particles. After that, the composite powders were calcined at 750 °C under

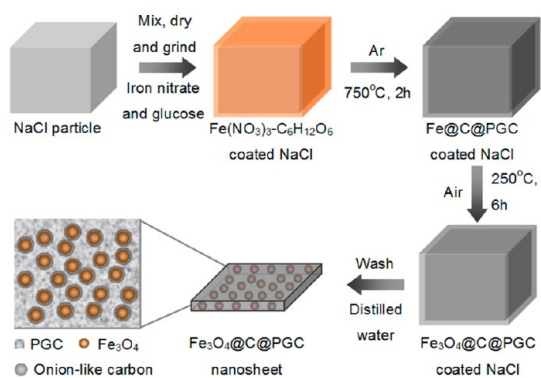**Figure 1. Schematic illustration of the *in situ* technique to fabricate 2D Fe$_3$O$_4$@C@PGC nanosheets by using the surface of NaCl particles as the template.**

Ar, and this seems to cause the metal precursor (Fe(NO$_3$)$_3$·9H$_2$O) to form iron oxide, and the carbon species from C$_6$H$_{12}$O$_6$ reduce iron oxide to Fe nanoparticles, which can catalyze the carbon from C$_6$H$_{12}$O$_6$ to form an encapsulating carbon layer around Fe nanoparticles or porous graphitic carbon. As a result, the coating layer on the surface of the NaCl particles was converted to carbon-encapsulated Fe nanoparticles embedded in a porous graphitic carbon nanosheet with uniform thickness. In the second step, the 2D Fe@C@PGC nanosheets were calcined in air to oxidize the Fe and thus yielded discrete and homogeneous carbon-encapsulated Fe$_3$O$_4$ nanoparticles embedded in porous graphitic carbon nanosheets. Finally, the obtained powder was treated with distilled water to dissolve the NaCl, and then pure Fe$_3$O$_4$@C@PGC nanosheets were obtained. The starting materials and the synthetic processes are both viable for large-scale production, making this approach particularly attractive for practical applications.

Figure 2a shows a typical low-magnification scanning electron microscopy (SEM) image of Fe@C@PGC nanosheets. Evidently, a large number of monodispersed and curved nanosheets with a lateral size from 1 μm to several micrometers and a large aspect ratio are well-dispersed in the sample. This 2D nanostructure is quite different from traditional porous carbon. Most porous carbon materials, especially hard carbons generated from the carbonization of saccharide or resin, are micrometer-sized blocks and monoliths.[17−19] It should be emphasized that, without the presence of NaCl, no 2D nanosheets were formed at the same conditions as those for the preparation of the Fe@C@PGC nanosheets. This result strongly indicates that the presence of NaCl plays an essential role in the formation of homogeneous 2D nanosheets. In order to clarify the effect of NaCl on the synthesis of Fe@C@PGC nanosheets, we have investigated the carbonization products of the mixture (Fe(NO$_3$)$_3$·9H$_2$O and C$_6$H$_{12}$O$_6$) without NaCl and the as-synthesized Fe@C@PGC products before removing the NaCl by using SEM

and transmission electron microscopy (TEM) analyses (as shown in Supporting Information Figures S1 and S2). As can be seen, the carbonization products synthesized without NaCl appear to be 3D micrometer-sized carbon blocks with Fe nanoparticles embedded, and no nanosheets can be observed in the products (Figure S1). When observing the SEM images (see Figure S2a,b) of the as-synthesized products before removing the NaCl, we further found that the Fe@C@PGC nanosheets were actually formed on the NaCl surface, indicating that the NaCl surface functions as the template to direct the formation of the 2D nanosheets. In general, the carbonization of glucose results in the formation of carbon blocks (see Figure S1a,b) other than carbon nanosheets due to the three-dimensional cross-linked structure. In this work, the addition of a mass of NaCl could provide their surface to direct the formation of Fe(NO$_3$)$_3$-C$_6$H$_{12}$O$_6$ complex coating and thus alter the three-dimensional cross-linkage state of the glucose during the curing process, which would result in the occurrence of a 2D nanostructure after carbonization. It is also found that the thickness and size of the nanosheets, or the size and content of the metal, can be tuned by adjusting the experimental parameters, such as the content and size of the NaCl and ratio of metal precursor to carbon precursor. With a higher content and larger size of NaCl, thinner and larger nanosheets can be obtained. Meanwhile, higher ratio of metal precursor to carbon precursor would lead to larger size and content of metal nanopartices within the nanosheets. Figure 2b−d presents typical TEM images of Fe@C@PGC nanosheets; it is obvious that these micrometer-sized nanosheets appear as a foam-like porous graphitic structure with many black Fe nanoparticles (see Figure S2c,d) homogeneously embedded. Moreover, these Fe nanoparticles are entirely encapsulated by thin onion-like carbon layers within porous graphitic carbon nanosheets (Figure 2d and Figure S2c).

After careful annealing under air, the Fe@C@PGC nanosheets can be oxidized and converted to Fe$_3$O$_4$@C@PGC nanosheets, which was confirmed by the following X-ray diffraction (XRD) analysis and electron microscope observations. As shown in Figure 2e, XRD patterns can clearly reveal the overall transitional process. From bottom to top, two distinct XRD patterns correspond to α-Fe (JCPDS 06-0696) and magnetite (JCPDS 19-0629) in sequence, implying the total conversion from the precursor (Fe@C@PGC nanosheets) to the targeted sample (Fe$_3$O$_4$@C@PGC nanosheets) by annealing under air. For the carbon in the Fe$_3$O$_4$@C@PGC nanosheets, the interplanar distance of d_{002} obtained from the (002) peak is about 0.342 nm, indicating that the carbon in the nanosheets should have a well-developed graphitic structure.[17,21,27] The average particle size of Fe$_3$O$_4$ nanoparticles in the nanosheets was calculated from the largest diffraction
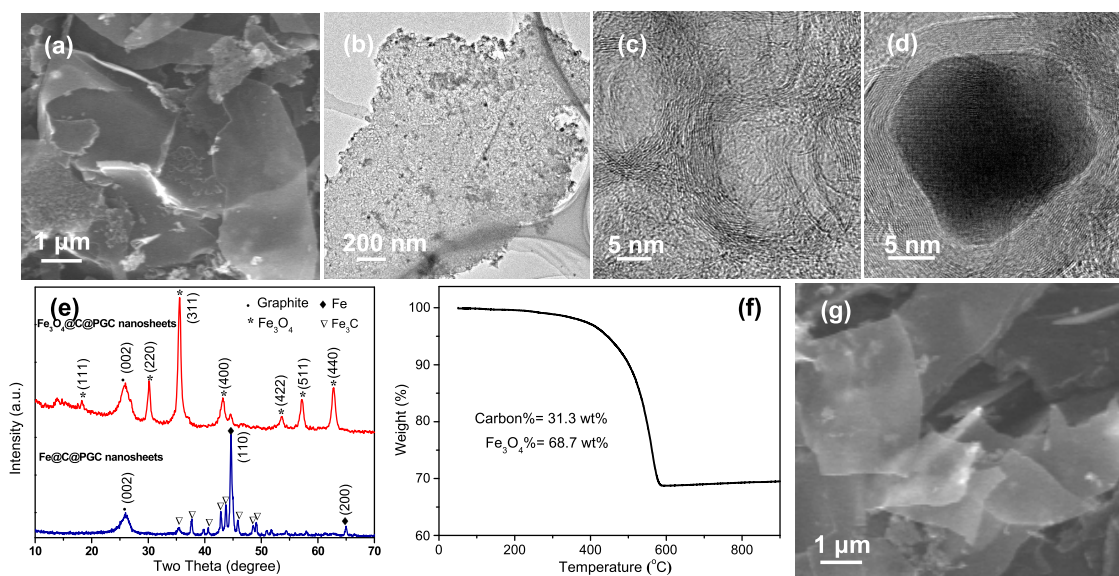
Figure 2. (a) SEM, (b) TEM, (c,d) HRTEM images of Fe@C@PGC nanosheets. (e) XRD patterns of the Fe@C@PGC nanosheets and Fe₃O₄@C@PGC nanosheets. (f) TGA profile and (g) SEM image of Fe₃O₄@C@PGC nanosheets.

peak (311) by using Scherrer's formula, and the estimated average crystal size is about 18.2 nm for Fe_3O_4 nanoparticles. Thermogravimetric analysis (TGA), carried out in air at a heating rate of 10 °C/min, was used to determine the chemical composition of the Fe_3O_4@C@PGC nanosheets (Figure 2f). The sample is heated to 900 °C so that Fe_3O_4 is oxidized to Fe_2O_3 and carbon is oxidized to CO_2. According to the remaining weight (of Fe_2O_3), the original fraction of Fe_3O_4 is calculated to be 68.7% by weight.

SEM (Figure 2g and Figure S3a) and TEM (Figure 3a–c and Figure S3b) characterizations show that the 2D porous morphology of the Fe@C@PGC nanosheets can be well-maintained for the Fe_3O_4@C@PGC nanosheets after annealing under air. Furthermore, many of these Fe_3O_4@C@PGC nanosheets exhibit a curved characteristic and a low contrast, revealing a very thin thickness (less than 30 nm) of the nanosheets (see Figure 2g and Figure S3a). Compared with 3D carbon-based blocks,[17−19] this special 2D nanosheet-type morphology can greatly facilitate the diffusion of both electrons and lithium ions because the thickness decreases from micrometer to nanometer in one dimension. High-magnification TEM (HRTEM) images (Figure 3d,e) of Fe_3O_4@C@PGC nanosheets clearly reveal that the porous carbon presents a very high degree of graphitization and the Fe_3O_4 nanoparticles (5−25 nm) are highly crystallized and perfectly encapsulated by thin and well-graphitized onion-like carbon shells within the nanosheets, in agreement with the above XRD results. The lattice fringe orientations in the HRTEM image (Figure 3e) demonstrate clear shell lattice fringes with d-spacings of 0.34 nm and core lattice fringes with d-spacings of 0.25 nm, which are in good agreement with that of the (002) planes of

graphite and the (311) plane of bulk Fe_3O_4, respectively. Energy-dispersive X-ray (Figure S3c) and selected area electronic diffraction (SAED) (Figure S3d) investigations further verify the encapsulated core being Fe_3O_4 nanoparticle.

In order to further confirm if our synthesized Fe_3O_4@C@PGC nanosheets have a high-quality encapsulation structure, a surface-sensitive high-resolution X-ray photoelectron spectroscopic (XPS) experiment was performed to examine the chemical characteristics of the surface of the nanosheets. Figure 3f shows a typical full XPS spectrum of the Fe_3O_4@C@PGC nanosheets, in which the photoelectron lines at a binding energy of about 285 and 532 eV are attributed to C 1s and O 1s, respectively, but there is almost an absence of the signals of Fe $2p_{3/2}$ and Fe $2p_{1/2}$ at about 710 and 724 eV, respectively. Because the atomic sensitivity factor of Fe is much higher than those of C and O, absence of its peaks implies that, in our synthesized Fe_3O_4@C@PGC nanosheets, the Fe_3O_4 appears to be completely sealed inside the carbon shells.[20,37]

The as-obtained Fe_3O_4@C@PGC nanosheets were also characterized by electrical conductivity measurement and Raman spectroscopy in detail to further validate the presence of well-graphitized carbon in the nanosheets. Electrical conductivity of the nanosheets was measured to be 1.2×10^2 S/cm. Raman spectrum (Figure 3g) obtained for the nanosheets presents two distinguishable peaks at about 1340 cm^{-1} (D-band) and 1596 cm^{-1} (G-band). The former band (D-band) is associated with disorder, allowing zone edge modes of the graphite structure to become active due to the lack of long-range order in amorphous and quasi-crystalline forms of carbon materials. The latter band (G-band) corresponds to the E_{2g} mode (stretching vibrations) in the basal plane of the crystalline
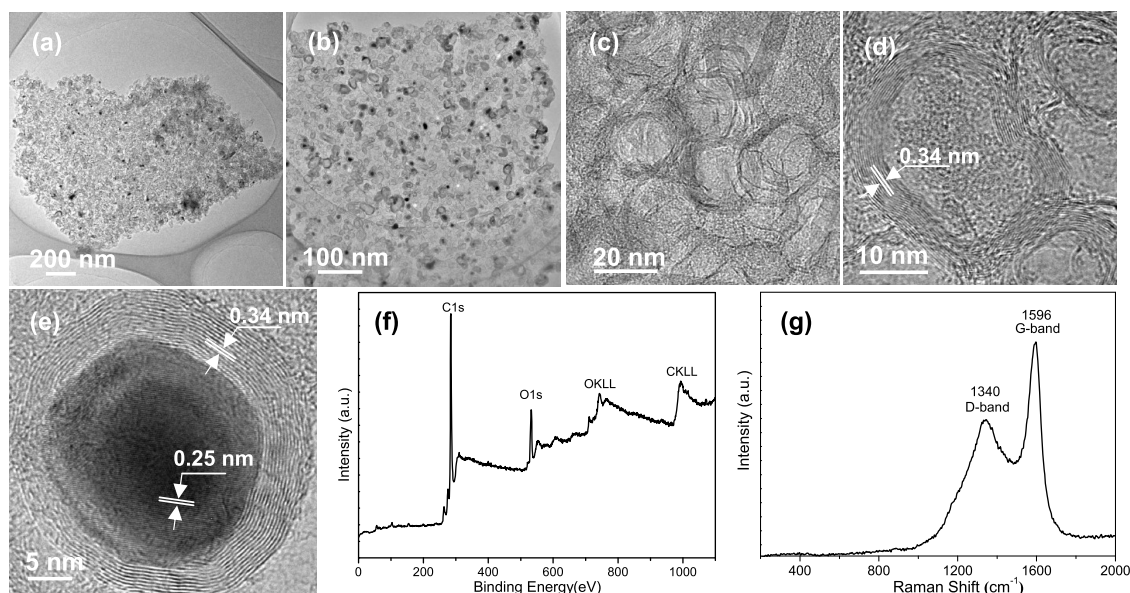
Figure 3. (a−c) Low-magnification TEM images, (d,e) high-magnification TEM images, (f) XPS spectrum, and (g) Raman spectrum of 2D Fe_3O_4@C@PGC nanosheets.

graphite. The peak intensity ratio between D- and G-bands (I_D/I_G) generally provides a useful index for comparing the degree of crystallinity of various carbon materials, that is, the smaller the ratio of I_D/I_G, the higher the degree of ordering in the carbon material. The I_D/I_G ratio for our Fe_3O_4@C@PGC nanosheets was calculated to be ~0.51, demonstrating a high graphitic crystallinity of carbon in the nanosheets,[17,21,27] which will be very beneficial for achieving better electronic conduction between adjacent Fe_3O_4 nanoparticles. Nitrogen adsorption−desorption measurements are carried out at 77 K to study the textural characteristics of the Fe_3O_4@C@PGC nanosheets. As shown in Figure S4a, the isotherm profile of the sample can be categorized as type IV with a large hysteresis loop observed at a relative pressure of $p/p_0 \approx 0.45-0.97$, implying a narrow mesopore diameter distribution and the existence of a large number of mesopores. In addition, another N_2 uptake is observed at a relatively high pressure of 0.97−1.0, which can be attributed to the presence of macropores. Meanwhile, the isotherms also suggested that there are micropores in the sample. The above results can be further verified by the pore size distribution in Figure S4b. The BET specific surface area is measured to be ~470 m²/g, which is much higher than that of commercial Fe_3O_4 nanoparticles (about 2 m²/g) and 3D Fe_3O_4/C composite (~168.8 m²/g, as shown in Figure S4c). The pore size distribution of the nanosheets (Figure S4b) lies in 1−235 nm range and shows the preponderance of ~3.7 nm mesopores. The above evidence demonstrates that the well-graphitized carbon with high electrical conductivity may be very beneficial for fast electron transport, and a large surface area and well-developed 2D porous structures of macropores and

mesopores may be very favorable to the electrolyte ion diffusion to active sites with less resistance and may accommodate huge volume changes of the Fe_3O_4@C nanoparticles during lithium ion insertion/extraction.[24,27]

The successful fabrication of the 2D Fe_3O_4@C@PGC nanosheets for a superior LIB anode is evident from the extraordinarily excellent electrochemical behavior (as shown in Figure 4). Figure 4a shows the first four cyclic voltammogram (CV) curves of the Fe_3O_4@C@PGC composite electrode at room temperature between 0.0 and 3.0 V at a scan rate of 0.1 mV/s. In agreement with literature,[17,19,27] it is clear that the CV curve of the first cycle is quite different from those of subsequent cycles, especially for the discharge branch. In the first discharge cycle, two well-defined peaks are observed at 0.97 and 0.60 V (vs Li^+/Li), which is usually ascribed to the occurrence of side reactions on the electrode surfaces and interfaces due to SEI formation, as well as the two steps of the lithiation reactions of Fe_3O_4 (step 1, $Fe_3O_4 + 2Li^+ + 2e^- \rightarrow Li_2(Fe_3O_4)$; and step 2, $Li_2(Fe_3O_4) + 6Li^+ + 6e^- \rightarrow 3Fe^0 + 4Li_2O$).[17,19,27] In comparison, the distinct peaks appear at 0.81 V during discharge and at 1.65 and 1.90 V during charge from the second cycle onward, exclusively corresponding to the electrochemical reduction/oxidation ($Fe_3O_4 \leftrightarrow Fe$) reactions accompanying lithium ion insertion (lithiation) and extraction (delithiation), in accord with those previously reported in the literature for Fe_3O_4-based electrodes.[17,19,27] Apparently, the peak intensity drops significantly in the second cycle, indicating the occurrence of some irreversible reactions with formation of an SEI film. Importantly, it is noteworthy that, after the first cycle, the voltage−current curves almost overlapped, which indicates that a stable SEI film formed on the surfaces and interfaces of onion-like carbon shells
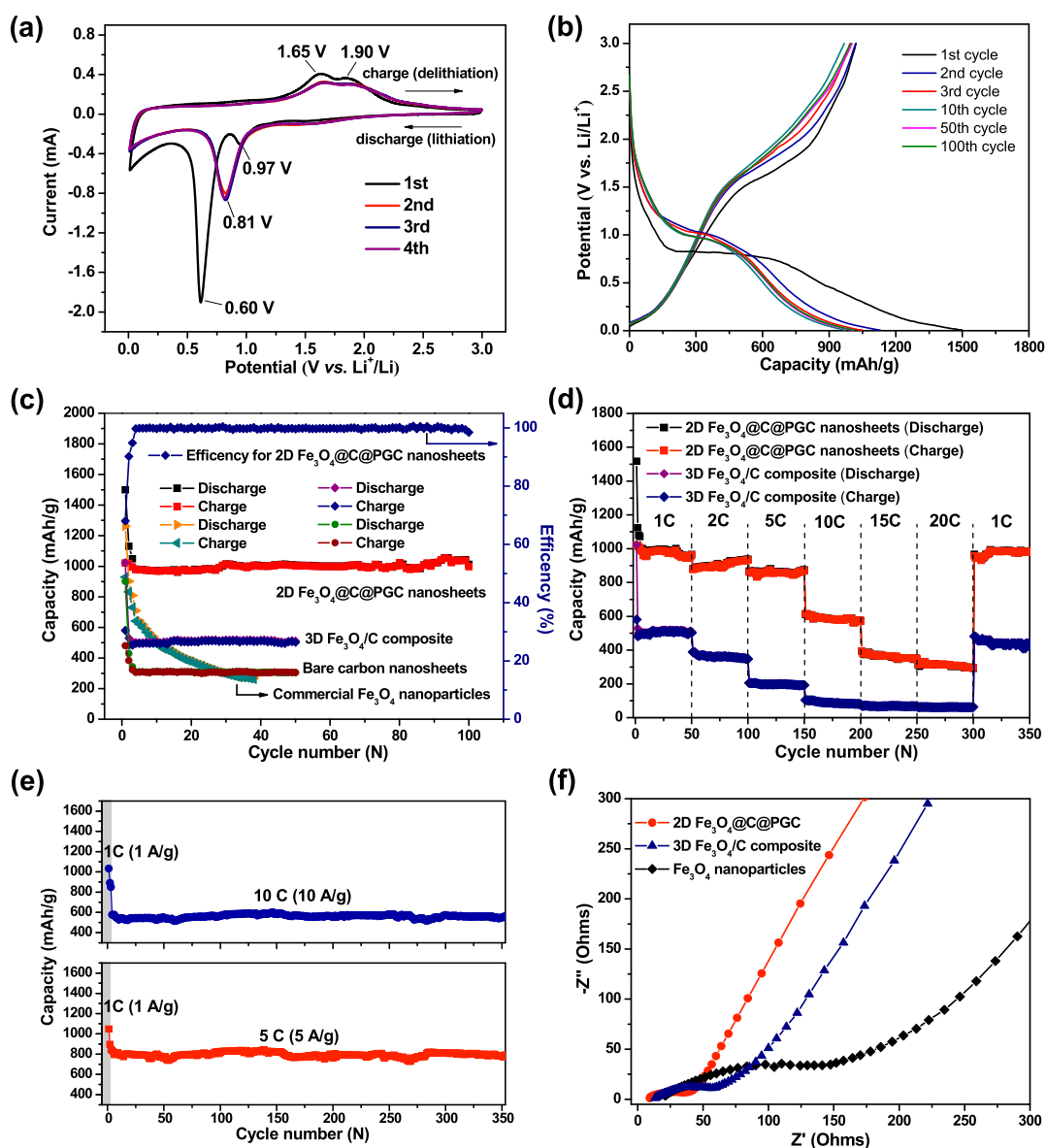
Figure 4. (a) Representative CV curves of an electrode based on the Fe_3O_4@C@PGC nanosheets obtained at a voltage range of 0.0 to 3.0 V (vs Li^+/Li) and potential scan rate of 0.1 mV/s. (b) Voltage profiles plotted for the first, second, third, 10th, 50th, and 100th cycles of the Fe_3O_4@C@PGC composite electrode at a current density of 1 A/g. (c) Charge/discharge capacities of the Fe_3O_4@C@PGC nanosheets, 3D Fe_3O_4/C composite, commercial Fe_3O_4 nanoparticles, and bare carbon nanosheets at a current density of 1 A/g. (d) Charge/discharge capacity of the Fe_3O_4@C@PGC and 3D Fe_3O_4/C composite electrodes at various rates for 350 cycles. (e) Charge capacity of the Fe_3O_4@C@PGC composite electrode at rates of 5 C (5 A/g) and 10 C (10 A/g) for 350 cycles. (f) Nyquist plots of the Fe_3O_4@C@PGC nanosheets, 3D Fe_3O_4/C composite, and commercial Fe_3O_4 nanoparticles at fresh coin cells over the frequency range from 100 kHz to 0.01 Hz.

in the first cycle can prevent the direct contact of encapsulated Fe_3O_4 nanoparticles with electrolyte and safeguard the structural integrity of interior Fe_3O_4 during subsequent charge—discharge cycles, thus leading to the high Coulombic efficiency and the stable and superior reversibility of the sample.[17,19,27]

Figure 4b shows representative discharge/charge voltage profiles of Fe_3O_4@C@PGC nanosheets at a current density of 1 A/g between 0.005 and 3.00 V. It can be seen that the sample delivers a very high lithium storage capacity of 1499 mAh/g during the initial discharge process, but a relative low reversible

capacity of 1021 mAh/g is achieved, leading to an initial Coulombic efficiency of around 68%. The relatively low initial Coulombic efficiency may be caused by the irreversible capacity loss, including inevitable formation of SEI and decomposition of electrolyte, which are common to most anode materials.[5−42] This characteristic also agrees well with the CV results that the cathodic peaks are present in the first scan while absent afterward. The discharge voltage plateau at ∼0.82 V in the first cycle is different from those of other cycles at ∼1.0 V, further indicating that irreversible reactions occurred in the first cycle. It should be

emphasized that no obvious change in both charge and discharge profiles is observed even after 100 cycles, which further indicates that the Fe₃O₄@C@PGC nanosheets are extraordinarily stable during cycling.[36−39]

To highlight the superiority of the unique 2D Fe₃O₄@C@PGC nanosheets for anode materials of LIBs, we tested the cycle performance of the Fe₃O₄@C@PGC composite electrode at a current density of 1 A/g. For comparison, commercial Fe₃O₄ nanoparticles were also investigated under the same conditions, together with 3D Fe₃O₄/C composite produced without NaCl as a control. All results are compiled in Figure 4c. Apparently, the 2D Fe₃O₄@C@PGC composite electrode demonstrates a much better cyclic retention than that for the commercial Fe₃O₄ nanoparticles and a much higher reversible capacity than that for the 3D Fe₃O₄/C composite, with a high reversible capacity of 1003 mAh/g after 50 cycles and 998 mAh/g even after 100 cycles, which are about 98.2 and 97.7% of the initial capacity, respectively. Furthermore, their Coulombic efficiency rapidly increases from 68% for the first cycle to about 99% after three cycles and remains nearly 100% thereafter, which suggests a facile lithium insertion/extraction associated with efficient transport of ions and electrons in the electrodes. For the commercial Fe₃O₄ nanoparticles with an average diameter of about 20 nm, their capacity fades very rapidly during the course of the first few cycles. Compared to the Fe₃O₄@C@PGC nanosheets, a significant lower capacity of only 240 mAh/g is delivered at the end of the 40 cycles. This evidently proves that the remarkably positive effect of the unique 2D encapsulation structure of the Fe₃O₄@C@PGC nanosheets. For the 3D Fe₃O₄/C composite prepared without NaCl, it shows a much lower capacity (about 500 mAh/g) than that of the 2D Fe₃O₄@C@PGC nanosheets, but its cycling performance is very excellent, indicating that the 3D carbon block might be unfavorable to the lithium storage capacity of the Fe₃O₄ nanoparticles but be beneficial for improving the structural stability of the Fe₃O₄ nanoparticles. It has been reported that, during the charge−discharge process, the Fe₃O₄-based anode surface would be covered by a SEI film, which forms due to the reductive decomposition of the organic electrolyte.[19−27] For the Fe₃O₄@C@PGC nanosheets, the carbon shell and porous carbon nanosheets can allow for the Fe₃O₄ nanoparticles to expand upon lithiation without breaking the carbon shell. In addition, it is well-known that the lithium storage capacity of Fe₃O₄ is mainly achieved through the reversible conversion reaction between the lithium ion and Fe₃O₄, forming Fe nanocrystals dispersed in Li₂O matrix, and the carbon shell can prevent the formed Fe nanocrystals from catalyzing the decomposition of the outer SEI. This in turn allows for the growth of a stable SEI on the surface of the carbon shell and prevents the continual rupturing and re-formation of the SEI. After

the formation of a stable SEI, their capacity is maintained very well and thus the anode of Fe₃O₄@C@PGC nanosheets exhibits exceedingly excellent cycling performance.[23−28] However, in the case of bare Fe₃O₄ nanoparticles, the SEI will rupture due to the mechanical strain generated by the volume expansion/contraction during cycling or the catalyzing by the Fe nanocrystals formed during the lithium extraction processes, and thus the electrode surface would be cyclically exposed to the electrolyte, which results in continual formation of very thick SEI films and accordingly continual consuming of electrolyte. The cyclical rupture and growth of SEI can cause low Coulombic efficiency, higher resistance to ionic transport, and low electronic conductivity of the whole electrode. Therefore, the capacity of the anode of bare Fe₃O₄ nanoparticles decreases rapidly, and their cycling performance is remarkably worse than that of the 2D Fe₃O₄@C@PGC nanosheets.[4−6] As for the 3D Fe₃O₄/C composite prepared without NaCl, their much larger diffusion path of lithium ions and much lower BET surface area compared to that of 2D Fe₃O₄@C@PGC nanosheets are very unfavorable for the insertion of lithium ions, thereby leading to a much lower lithium storage capacity when compared with 2D Fe₃O₄@C@PGC nanosheets. In order to further elucidate the effect of the bare carbon nanosheets on the electrochemical performance of the 2D Fe₃O₄@C@PGC nanosheets, the cycling performance of the bare carbon nanosheets obtained by eliminating the Fe₃O₄ from the Fe₃O₄@C@PGC nanosheets was also investigated. As shown in Figure 4c, the bare carbon exhibits a very low reversible capacity of about 305 mAh/g, but its cycling performance is rather outstanding, which demonstrates that the bare carbon nanosheets might contribute little to the Li storage capacity of the Fe₃O₄@C@PGC nanosheets but be very favorable for improving the structural stability of the Fe₃O₄ nanoparticles.

As expected, the Fe₃O₄@C@PGC composite electrode exhibits an extremely durable high rate capability, as displayed in Figure 4d. It delivers a reversible capacity of 963 mAh/g when first cycled at 1 C for 50 cycles, 932 mAh/g at 2 C after 100 cycles, 868 mAh/g at 5 C after 150 cycles, and 570 mAh/g at 10 C after 200 cycles. Even at high rates of 15 and 20 C, the reversible capacities still retain approximately 349 and 297 mAh/g, respectively. Moreover, when the current rate was finally returned to its initial value of 1 C after a total of 300 cycles, a capacity of 956 mAh/g was still recoverable and sustainable up to the 350th cycle without any losses (980 mAh/g at the 350th cycle). Table S1 shows the average reversible capacities at different rates. As can be seen, the average reversible capacities of the Fe₃O₄@C@PGC nanosheets are 977 mAh/g when cycled at 1 C, 905 mAh/g at 2 C, 858 mAh/g at 5 C, 587 mAh/g at 10 C, 364 mAh/g at 15 C, 311 mAh/g at 20 C, and finally back to 975 mAh/g at 1 C. The results
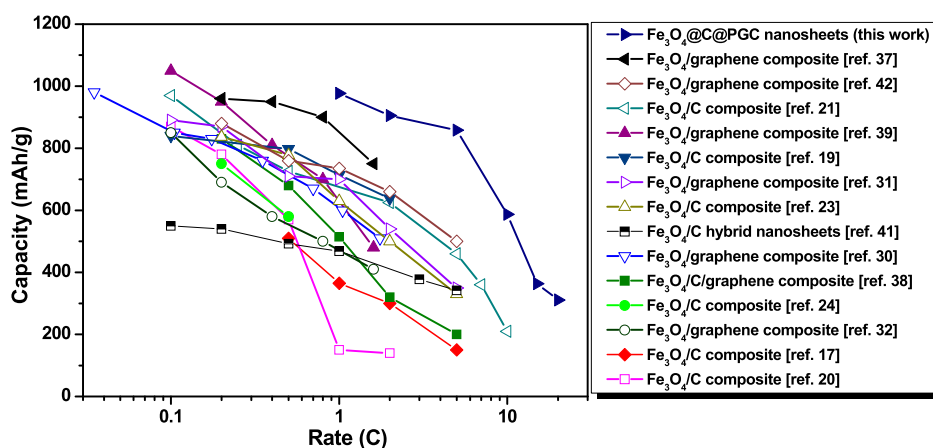
Figure 5. Comparison of capacity at different rates for 2D Fe_3O_4@C@PGC composite electrode with those of Fe_3O_4 nanostructure and Fe_3O_4/C composite anodes reported.

suggest that the structure of Fe_3O_4@C@PGC nanosheets remains exceedingly stable even under high rate cycling. In contrast, the control electrode of the 3D Fe_3O_4/C composite fabricated without using NaCl shows significantly lower capacity (as shown in Figure 4d and Table S1), which further verifies the advantages of using the 2D Fe_3O_4@C@PGC nanosheets for lithium storage. In order to further confirm the durability of this nanosheet anode to work at higher rates (5 and 10 C), Fe_3O_4@C@PGC composite electrode cyclability has been investigated upon 353 cycles and the evolution of the specific capacities is displayed in Figure 4e. Three cycles were first performed at 1 C and then 350 cycles at 5 or 10 C. It can be seen that the reversible capacities at 5 and 10 C rates are 836 and 576 mAh/g, respectively, in the initial cycle with a very slow capacity fade to 823 and 568 mAh/g, respectively, after 150 cycles, and then to 792 and 556 mAh/g, respectively, after 350 cycles, further demonstrating extraordinary superior cycling stability of this 2D structure even at high charge/discharge rates. Such superhigh rate performance and cycling stability at high charge/discharge rates are significantly higher than in previously reported works on Fe_3O_4 nanostructures and Fe_3O_4/carbon hybrids (as shown in Figure 5).[5−42] Indeed, the latter report usual maximum C rates of 5 C with capacities varying from 100[40] to 500 mAh/g[21,42] and exceptionally 10 C with capacities about 200 mAh/g.[21]

In order to clarify the difference in electrochemical performance among the 2D Fe_3O_4@C@PGC nanosheets, 3D Fe_3O_4/C composite, and commercial Fe_3O_4 nanoparticles, electrochemical impedance spectroscopy (EIS), a promising tool for investigating diffusion issues, was conducted at frequencies from 100 kHz to 0.01 Hz to identify the relationship between the electrochemical performance and electrode kinetics. Figure 4f shows the Nyquist plots for the 2D Fe_3O_4@C@PGC nanosheets, 3D Fe_3O_4/C composite, and commercial Fe_3O_4 nanoparticles at fresh coin cells, which share the common feature of a high-frequency

depressed semicircle and a medium-frequency depressed semicircle followed by a linear tail in the low-frequency region. Following are the common equivalent circuit descriptions of these features: the intercept on the Z' axis at the high-frequency end is the electrolyte resistance (R_s), the size of the semicircular that encompasses the medium-frequency response is an indication of the charge-transfer resistance (R_{ct}) in the electrode reaction, and the inclined line in the low-frequency region represents the Warburg impedance (Z_w) related to lithium diffusion in the solid.[29] Apparently, the diameter of the semicircle for 2D Fe_3O_4@C@PGC electrode in the high−medium-frequency region is significantly smaller than that of 3D Fe_3O_4/C composite and commercial Fe_3O_4 nanoparticles. This indicates that 2D Fe_3O_4@C@PGC composite electrodes possess lowest contact and charge-transfer impedances, which can lead to rapid electron transport during the electrochemical lithium insertion/extraction reaction and thus result in significant improvement on the rate performance.

The morphology and structure evolution of the Fe_3O_4@C@PGC composite anode under the severe volume expansion/contraction during lithium insertion/extraction were further investigated by TEM techniques. Figure S5 shows the TEM images of the Fe_3O_4@C@PGC anode after 350 charge/discharge cycles for rate performance test in Figure 4d. Compared with Figure 3a,b, the morphology of the Fe_3O_4@C@PGC after 350 charge/discharge cycles was similar to that of the pristine one, suggesting the robustness of the 2D nanostructure. Moreover, TEM images in Figure S6b−d show that the porous graphitic carbon, onion-like carbon shells, and the core−shell structures were still maintained after charge/discharge cycling, and the thickness of the carbon shells was similar to that before cycling. The similar morphology indicates that the Fe_3O_4@C@PGC anodes can effectively decrease substantial aggregation and cracking upon cycling, ensuring their extremely excellent electrochemical performance. In particular, 2D porous

graphite carbon nanosheets have good elasticity to effectively accommodate the mechanical stress caused by the large volume change of Fe_3O_4@C nanoparticles during the charge—discharge process.

As shown in the results presented above, our 2D Fe_3O_4@C@PGC composite electrode displays extremely superior electrochemical performance and structural stability. These outstanding properties should be attributed to their distinct structure and morphology that offer the following benefits: (1) the 2D porous nanosheet-type feature may ensure the short transport path for both electrons and lithium ions, leading to good conductivity and fast charge/discharge rates; (2) the thin onion-like carbon shells can protect the encapsulated Fe_3O_4 nanoparticles from directly contacting with the electrolyte and alleviate the side reactions at the interface between Fe_3O_4 and electrolyte, resulting in structural and interfacial stabilization of Fe_3O_4 nanoparticles. Moreover, good electrical conductivity of the outer carbon shells can complement the low conductivity of inner Fe_3O_4 cores; (3) the onion-like carbon shells of the Fe_3O_4@C nanoparticles are interconnected through the high-conducting PGC nanosheets, thus constructing a very efficient and continuous conductive network; (4) the 2D PGC nanosheets with excellent mechanical flexibility can efficiently inhibit the aggregation of Fe_3O_4 nanoparticles and circumvent the severe volume expansion/contraction of Fe_3O_4@C nanoparticles associated with lithium insertion/extraction and thus preserve the structural integrity of the whole electrode. As a result, their original textural properties in terms of shape, size, and structural integrity can be retained even after being charged/discharged over 350 cycles for rate performance test (as shown in Figure S5). Due to the enhanced structural stability and integrity and excellent kinetics for lithium ion and charge transport, the lithium storage properties of our 2D Fe_3O_4@C@PGC nanosheets are thus remarkably improved.

CONCLUSIONS

In summary, novel carbon-encapsulated Fe_3O_4 nanoparticles embedded in 2D porous graphitic carbon nanosheets (Fe_3O_4@C@PGC nanosheets) have been successfully fabricated by a facile and scalable *in situ* synthesis method with assistance of the surface of water-soluble NaCl particles. This unique hybrid nanostructure is made of very thin 2D porous graphitic carbon nanosheets with a thickness of less than 30 nm in which Fe_3O_4 nanoparticles ($\sim$18.2 nm) coated with conformal and thin onion-like carbon shells are homogeneously embedded. In this architecture, the thin onion-like carbon shells can effectively avoid the direct exposure of encapsulated Fe_3O_4 to the electrolyte and preserve the structural and interfacial stabilization of Fe_3O_4 nanoparticles. Meanwhile, the flexible and conductive 2D PGC nanosheets can accommodate the mechanical stress induced by the volume change of embedded Fe_3O_4@C nanoparticles as well as inhibit the aggregation of Fe_3O_4 nanoparticles and thus maintain the structural and electrical integrity of the Fe_3O_4@C@PGC electrode during the charge and discharge processes. As a result, such a 2D nanostructured electrode exhibits an extremely durable high-rate capability: a capacity of 858 mAh/g is achieved at 5 C, 587 mAh/g at 10 C, and 311 mAh/g at 20 C. The present 2D Fe_3O_4@C@PGC nanosheets are found to sustain very high C rates without any structural damaging. Cycling at 10 C after 350 cycles leads to a recovered capacity of 556 mAh/g, still 1.5 times the capacity of graphite, which is the best one ever reported for a Fe_3O_4-based electrode including various nanostructured Fe_3O_4 anode materials, composite electrodes, *etc*. Our results show that the 2D Fe_3O_4@C@PGC nanosheets are promising anode materials for the next generation LIBs with high energy and power density. Furthermore, this *in situ* and high-yield strategy for preparing Fe_3O_4@C@PGC nanosheets can also be extended to build a variety of other interesting carbon-encapsulated transition metal oxide nanoparticles uniformly embedded in 2D porous graphitic carbon nanosheets for important applications in high-performance LIBs, supercapacitors, adsorbents, catalysts, and sensors in many scientific disciplines.

METHODS

Synthesis of 2D Fe_3O_4@C@PGC Nanosheets. The reagents were obtained from commercial sources and used without further purification. For preparing 2D Fe_3O_4@C@PGC nanosheets, the metal precursors of $Fe(NO_3)_3 \cdot 9H_2O$ (0.73 g), glucose (2 g), and sodium chloride (15 g) were dissolved in 10 mL of deionized water. The resulting mixed solution was dried in a drying oven at 80 °C for 24 h and then ground by agate mortar to obtain very fine composite powders. After that, the composite powders were heated at 750 °C for 2 h in a tube furnace under flowing Ar atmosphere (50 mL/min) to obtain 2D Fe@C@PGC nanosheets and then annealed at 250 °C for 6 h under air. Once cooled to room temperature, the obtained powder was treated with deionized water to dissolve the sodium chloride and then pure 2D Fe_3O_4@C@PGC nanosheets were obtained. For comparison, 3D Fe_3O_4/C composites were also

synthesized by carbonizing the mixture of $Fe(NO_3)_3 \cdot 9H_2O$ and glucose without NaCl at the same conditions as those for the preparation of the Fe_3O_4@C@PGC nanosheets.

Characterization Techniques. Transmission electron microscope (TEM) and high-resolution TEM (HRTEM) were performed on a FEI Tecnai G^2 F20 TEM. Raman spectra were recorded on the LabRAM HR Raman spectrometer using laser excitation at 514.5 nm from an argon ion laser source. X-ray diffraction (XRD) measurements were taken on a Rigaku D/max diffractometer with Cu Kα radiation. Thermogravimetric analysis (TGA) was performed with a Perkin-Elmer (TA Instruments) up to 800 °C at a heating rate of 10 °C/min in air. The electrical conductivity was measured by a four-electrode method using a conductivity detection meter (Shanghai Fortune Instrument, FZ-2010). Brunauer—Emmett—Teller (BET) surface areas and porosities

of the products were determined by nitrogen adsorption and desorption using a Micromeritics ASAP 2020 analyzer. X-ray photoelectron spectroscopic (XPS) measurement of the $Fe_3O_4@C@PGC$ nanosheets was made on a PHI1600 ESCA system.

Electrochemical Measurement. The working electrodes were made through the following steps: active materials ($Fe_3O_4@C@PGC$ nanosheets, 3D Fe_3O_4/C composite, bare carbon nanosheets, or Fe_3O_4 nanoparticles with average diameter of about 20 nm purchased from DK nanotechnology Co. LTD, Beijing), conductivity agent (carbon black), and binder (polyvinylidene fluoride, PVDF) in a weight ratio of 80:10:10 were blended with N-methylpyrrolidone as solvent. Electrode film prepared by coating the mixture on a copper foil was first vacuum-dried at 80 °C for 4 h and then at 120 °C for 12 h. Coin cells (CR2032) were fabricated using lithium metal as the counter electrode, Celgard 2400 as the separator, and $LiPF_6$ (1 M) in ethylene carbonate/dimethyl carbonate/diethyl carbonate (EC/DMC/DEC, 1:1:1 vol %) as the electrolyte. The assembly of the cell was conducted in an Ar-filled glovebox followed by an overnight aging treatment before the test. Cyclic voltammetry (CV) measurement was conducted at 0.1 mV/s within the range of 0.0–3.0 V on a CHI660D electrochemical workstation. The cycle life and rate capability of the cells were tested within a fixed voltage window of 0.005–3.00 V (vs Li^+/Li) by using a battery testing system (LAND CT 2001A, China). All of the specific capacities here were calculated on the basis of the total weight of the $Fe_3O_4@C@PGC$ nanosheets, 3D Fe_3O_4/C composite, commercial Fe_3O_4 nanoparticles, or bare carbon nanosheets.

Conflict of Interest: The authors declare no competing financial interest.

Supporting Information Available: Supplementary SEM and TEM images, EDS, SAED, and BET analyses. This material is available free of charge *via* the Internet at http://pubs.acs.org.

REFERENCES AND NOTES

1. Dunn, B.; Kamath, H.; Tarascon, J. M. Electrical Energy Storage for the Grid: A Battery of Choices. *Science* **2011**, *334*, 928–935.

2. Xin, X.; Zhou, X. F.; Wu, J. H.; Yao, X. Y.; Liu, Z. P. Scalable Synthesis of TiO_2/Graphene Nanostructured Composite with High-Rate Performance for Lithium Ion Batteries. *ACS Nano* **2012**, *6*, 11035–11043.

3. Taberna, P. L.; Mitra, S.; Poizot, P.; Simon, P.; Tarascon, J. M. High Rate Capabilities Fe_3O_4-Based Cu Nano-Architectured Electrodes for Lithium-Ion Battery Applications. *Nat. Mater.* **2006**, *5*, 567–573.

4. Poizot, P.; Laruelle, S.; Grugeon, S.; Dupont, L.; Tarascon, J. M. Nano-Sized Transition-Metal Oxides as Negative-Electrode Materials for Lithium-Ion Batteries. *Nature* **2000**, *407*, 496–499.

5. Arico, A. S.; Bruce, P.; Scrosati, B.; Tarascon, J. M.; Van Schalkwijk, W. Nanostructured Materials for Advanced Energy Conversion and Storage Devices. *Nat. Mater.* **2005**, *4*, 366–377.

6. Guo, Y. G.; Hu, J. S.; Wan, L. J. Nanostructured Materials for Electrochemical Energy Conversion and Storage Devices. *Adv. Mater.* **2008**, *20*, 2878–2887.

7. Kang, N.; Park, J. H.; Choi, J.; Jin, J.; Chun, J.; Jung, I. G.; Jeong, J.; Park, J. G.; Lee, S. M.; Kim, H. J.; *et al.* Nanoparticulate Iron Oxide Tubes from Microporous Organic Nanotubes as Stable Anode Materials for Lithium Ion Batteries. *Angew. Chem. Int. Ed.* **2012**, *51*, 6626–6630.

8. Wang, Z. Y.; Zhou, L.; Lou, X. W. Metal Oxide Hollow Nanostructures for Lithium-Ion Batteries. *Adv. Mater.* **2012**, *24*, 1903–1911.

9. Xu, X. D.; Cao, R. G.; Jeong, S. K.; Cho, J. Spindle-like Mesoporous α-Fe_2O_3 Anode Material Prepared from MOF Template for High-Rate Lithium Batteries. *Nano Lett.* **2012**, *12*, 4988–4991.

10. Balaya, P.; Li, H.; Kienle, L.; Maier, J. Fully Reversible Homogeneous and Heterogeneous Li Storage in RuO_2 with High Capacity. *Adv. Funct. Mater.* **2003**, *13*, 621–625.

11. Cui, Z. M.; Jiang, L. Y.; Song, W. G.; Guo, Y. G. High-Yield Gas-Liquid Interfacial Synthesis of Highly Dispersed Fe_3O_4 Nanocrystals and Their Application in Lithium-Ion Batteries. *Chem. Mater.* **2009**, *21*, 1162–1166.

12. Liu, C.; Li, F.; Ma, L.-P.; Cheng, H.-M. Advanced Materials for Energy Storage. *Adv. Mater.* **2010**, *22*, E28–E62.

13. Peng, C. X.; Chen, B. D.; Qin, Y.; Yang, S. H.; Li, C. Z.; Zuo, Y. H.; Liu, S. Y.; Yang, J. H. Facile Ultrasonic Synthesis of CoO Quantum Dot/Graphene Nanosheet Composites with High Lithium Storage Capacity. *ACS Nano* **2012**, *6*, 1074–1081.

14. Yang, S. B.; Feng, X. L.; Ivanovici, S.; Mullen, K. Fabrication of Graphene-Encapsulated Oxide Nanoparticles: Towards High-Performance Anode Materials for Lithium Storage. *Angew. Chem. Int. Ed.* **2010**, *49*, 8408–8411.

15. Zhu, X. J.; Zhu, Y. W.; Murali, S.; Stoller, M. D.; Ruoff, R. S. Nanostructured Reduced Graphene Oxide/Fe_2O_3 Composite as a High-Performance Anode Material for Lithium Ion Batteries. *ACS Nano* **2011**, *5*, 3333–3338.

16. Zhou, G. M.; Wang, D. W.; Yin, L. C.; Li, N.; Li, F.; Cheng, H. M. Oxygen Bridges between NiO Nanosheets and Graphene for Improvement of Lithium Storage. *ACS Nano* **2012**, *6*, 3214–3223.

17. Yang, Z. C.; Shen, J. G.; Archer, L. A. An *In Situ* Method of Creating Metal Oxide–Carbon Composites and Their Application as Anode Materials for Lithium-Ion Batteries. *J. Mater. Chem.* **2011**, *21*, 11092–11097.

18. Yang, Z. C.; Shen, J. G.; Jayaprakash, N.; Archer, L. A. Synthesis of Organic–Inorganic Hybrids by Miniemulsion Polymerization and Their Application for Electrochemical Energy Storage. *Energy Environ. Sci.* **2012**, *5*, 7025–7032.

19. Piao, Y. Z.; Kim, H. S.; Sung, Y. E.; Hyeon, T. Facile Scalable Synthesis of Magnetite Nanocrystals Embedded in Carbon Matrix as Superior Anode Materials for Lithium-Ion Batteries. *Chem. Commun.* **2010**, *46*, 118–120.

20. Yoon, T.; Chae, C.; Sun, Y. K.; Zhao, X.; Kung, H. H.; Lee, J. K. Bottom-Up *In Situ* Formation of Fe_3O_4 Nanocrystals in a Porous Carbon Foam for Lithium-Ion Battery Anodes. *J. Mater. Chem.* **2011**, *21*, 17325–17330.

21. Kang, E.; Jung, Y. S.; Cavanagh, A. S.; Kim, G. H.; George, S. M.; Dillon, A. C.; Kim, J. K.; Lee, J. Fe_3O_4 Nanoparticles Confined in Mesocellular Carbon Foam for High Performance Anode Materials for Lithium-Ion Batteries. *Adv. Funct. Mater.* **2011**, *21*, 2430–2438.

22. Chen, J. S.; Zhang, Y. M.; Lou, X. W. One-Pot Synthesis of Uniform Fe_3O_4 Nanospheres with Carbon Matrix Support for Improved Lithium Storage Capabilities. *ACS Appl. Mater. Interfaces* **2011**, *3*, 3276–3279.

23. Liu, J.; Zhou, Y.; Liu, F.; Liu, C.; Wang, J.; Pana, Y.; Xue, D. One-Pot Synthesis of Mesoporous Interconnected Carbon-Encapsulated Fe_3O_4 Nanospheres as Superior Anodes for Li-Ion Batteries. *RSC Adv.* **2012**, *2*, 2262–2265.

24. Zhang, W. M.; Wu, X. L.; Hu, J. S.; Guo, Y. G.; Wan, L. J. Carbon Coated Fe_3O_4 Nanospindles as a Superior Anode Material for Lithium-Ion Batteries. *Adv. Funct. Mater.* **2008**, *18*, 3941–3946.

25. Muraliganth, T.; Murugan, A. V.; Manthiram, A. Facile Synthesis of Carbon-Decorated Single-Crystalline Fe_3O_4 Nanowires and Their Application as High Performance Anode in Lithium Ion Batteries. *Chem. Commun.* **2009**, 7360–7362.

26. Lee, J. E.; Yu, S. H.; Lee, D. J.; Lee, D. C.; Han, S. I.; Sung, Y. E.; Hyeon, T. Facile and Economical Synthesis of Hierarchical Carbon-Coated Magnetite Nanocomposite Particles and Their Applications in Lithium Ion Battery Anodes. *Energy Environ. Sci.* **2012**, *5*, 9528–9533.

27. Zhu, T.; Chen, J. S.; Lou, X. W. Glucose-Assisted One-Pot Synthesis of FeOOH Nanorods and Their Transformation to Fe$_3$O$_4$@Carbon Nanorods for Application in Lithium Ion Batteries. *J. Phys. Chem. C* **2011**, *115*, 9814–9820.

28. Wu, P.; Du, N.; Zhang, H.; Yu, J. X.; Yang, D. R. Carbon Nanocapsules as Nanoreactors for Controllable Synthesis of Encapsulated Iron and Iron Oxides: Magnetic Properties and Reversible Lithium Storage. *J. Phys. Chem. C* **2011**, *115*, 3612–3620.

29. Wang, J. Z.; Zhong, C.; Wexler, D.; Idris, N. H.; Wang, Z. X.; Chen, L. Q.; Liu, H. K. Graphene-Encapsulated Fe$_3$O$_4$ Nanoparticles with 3D Laminated Structure as Superior Anode in Lithium Ion Batteries. *Chem.—Eur. J.* **2011**, *17*, 661–667.

30. Zhou, G. M.; Wang, D. W.; Li, F.; Zhang, L. L.; Li, N.; Wu, Z. S.; Wen, L.; Lu, G. Q.; Cheng, H. M. Graphene-Wrapped Fe$_3$O$_4$ Anode Material with Improved Reversible Capacity and Cyclic Stability for Lithium Ion Batteries. *Chem. Mater.* **2010**, *22*, 5306–5313.

31. Liu, J. H.; Liu, X. W. Two-Dimensional Nanoarchitectures for Lithium Storage. *Adv. Mater.* **2012**, *24*, 4097–4111.

32. Baek, S.; Yu, S. H.; Park, S. K.; Pucci, A.; Marichy, C.; Lee, D. C.; Sung, Y. E.; Piao, Y. Z.; Pinna, N. A One-Pot Microwave-Assisted Non-aqueous Sol−Gel Approach to Metal Oxide/Graphene Nanocomposites for Li-Ion Batteries. *RSC Adv.* **2011**, *1*, 1687–1690.

33. Qu, Q.; Yang, S.; Feng, X. 2D Sandwich-like Sheets of Iron Oxide Grown on Graphene as High Energy Anode Material for Supercapacitors. *Adv. Mater.* **2011**, *23*, 5574–5580.

34. Zhou, J. S.; Song, H. H.; Ma, L. L.; Chen, X. H. Magnetite/Graphene Nanosheet Composites: Interfacial Interaction and Its Impact on the Durable High-Rate Performance In Lithium-Ion Batteries. *RSC Adv.* **2011**, *1*, 782–791.

35. Zhou, W. W.; Zhu, J. X.; Cheng, C. W.; Liu, J. P.; Yang, H. P.; Cong, C. X.; Guan, C.; Jia, X. T.; Fan, H. J.; Yan, Q. Y.; *et al.* A General Strategy toward Graphene@Metal Oxide Core−Shell Nanostructures for High-Performance Lithium Storage. *Energy Environ. Sci.* **2011**, *4*, 4954–4961.

36. Kim, I. T.; Magasinski, A.; Jacob, K.; Yushin, G.; Tannenbaum, R. Synthesis and Electrochemical Performance of Reduced Graphene Oxide/Maghemite Composite Anode for Lithium Ion Batteries. *Carbon* **2013**, *52*, 56–64.

37. Chen, W. F.; Li, S. R.; Chen, C. H.; Yan, L. F. Self-Assembly and Embedding of Nanoparticles by *In Situ* Reduced Graphene for Preparation of a 3D Graphene/Nanoparticle Aerogel. *Adv. Mater.* **2011**, *23*, 5679–5683.

38. Li, B. J.; Cao, H. Q.; Shao, J.; Qu, M. Z. Enhanced Anode Performances of the Fe$_3$O$_4$−Carbon−rGO Three Dimensional Composite in Lithium Ion Batteries. *Chem. Commun.* **2011**, *47*, 10374–10376.

39. Su, J.; Cao, M. H.; Ren, L.; Hu, C. W. Fe$_3$O$_4$ Graphene Nanocomposites with Improved Lithium Storage and Magnetism Properties. *J. Phys. Chem. C* **2011**, *115*, 14469–14477.

40. Li, B. J.; Cao, H. Q.; Shao, J.; Qu, M. Z.; Warner, J. H. Superparamagnetic Fe$_3$O$_4$ Nanocrystals@Graphene Composites for Energy Storage Devices. *J. Mater. Chem.* **2011**, *21*, 5069–5075.

41. Jang, B.; Park, M.; Chae, O. B.; Park, S.; Kim, Y.; Oh, S. M.; Piao, Y.; Hyeon, T. Direct Synthesis of Self-Assembled Ferrite/Carbon Hybrid Nanosheets for High Performance Lithium-Ion Battery Anodes. *J. Am. Chem. Soc.* **2012**, *134*, 15010–15015.

42. Su, Y. Z.; Li, S.; Wu, D. Q.; Zhang, F.; Liang, H. W.; Gao, P. F.; Cheng, C.; Feng, X. L. Two-Dimensional Carbon-Coated Graphene/Metal Oxide Hybrids for Enhanced Lithium Storage. *ACS Nano* **2012**, *6*, 8349–8356.